Ring resonator-based highly sensitive chemical/biochemical sensor created on holes in silicon slab 2D photonic crystal

Puja Sharma[1] · Sarang Medhekar[1]

Abstract 2D photonic crystal ring resonator (2DPCRR)-based highly sensitive chemical/biochemical sensor is designed and simulated. It consists of triangular lattice air holes on a silicon slab of refractive index 3.46. The sensitivity is determined by shifts in the resonance wavelength as a function of the refractive index of sensing holes. Simulations are performed using the two-dimension finite-difference time-domain method, and the band diagram is calculated using the plane wave expansion method. The 2DPCRR has ultra-compact footprint of $75\mu m^2$, high-quality factor of 3105.58, with a spectral width of 0.5nm at the resonant wavelength of 1552.79nm. Sensor shows a high figure of merit ($862RIU^{-1}$), a low detection limit ($1.2 * 10^{-4}RIU$), and a maximum sensitivity of 431nm/RIU. The proposed sensor exhibits considerable performance enhancements in comparison with previously published results.

Introduction

Photonic crystals (PCs) are periodic dielectric nanostructures engineered for controlling and manipulating electromagnetic waves. PCs allow for truly practicable all-optical devices because of their tremendous ability to control light propagation in ultra-small dimensions [1]. PCs are classified as one, two, or three-dimensional based on refractive index modulation in one, two, and three dimensions. Refractive index modulation results in a forbidden frequency range known as the photonic bandgap (PBG). Periodicity of the PCs can be modified to localize light in a small mode volume by introducing point and line defects [2].

PCs structures are of two types: (1) rods in the air and (2) holes in the slab. Among these, holes in slab-based devices provide remarkable flexibility for sensor design. In contrast to rod-type structures, removal of the background material beneath the PCs is possible in slabs to create favourable conditions for reducing vertical light leakage [3]. Further, larger contrast between the silicon slab and air holes enables substantial confinement of light within the slab, allowing for symmetric light propagation in the z-direction perpendicular to the slab plane. Microstructure photonic sensors (or PCs sensors) have received significant attention in recent years as they allow for ultra-compact size, lightweight, low power, quick response, and accurate detection [4]. In general, chemical or biological analytes are identified in a sensor either by (i) label-free sensing or (ii) fluorescence detection techniques. Label-free sensing detects the target biological analyte in its natural state [5], whereas fluorescent-based detection labels the biological molecules first and then detects the intensity of the fluorescence [6]. PCs sensors offer label-free sensing [7]. PCs sensors are primarily based on the refractive index change mechanism [8]. The shift in the resonance wavelength can be seen by infusing various chemical or biological substances into the sensing region [9]. Different refractive index-based sensors [10] are reported in the literature. The current work, however, is focused on chemical/biochemical sensors that have potential applications in both environmental and biological monitoring.

PCs-based sensors existing in the literature are based on (i) ring resonators [8], holes in slab-based waveguides [11],

✉ Sarang Medhekar
sarang.medhekar@cuj.ac.in; smedhekarbit@gmail.com

1 Department of Physics, Central University of Jharkhand, Ranchi 835222, India

Mach–Zehnder interferometer (MZI)[12], and microcavities [13]. Many PC-based sensors have recently been published in the literature, including temperature sensors [13], pressure sensors [14], humidity sensors [15], and biosensors [16], etc. Chemical/biological sensor has huge number of applications in (i) petrochemical industry, (ii) industrial safety, (iii) biomedicine/biological sensing, (v) environmental sensing, (vi) food testing, (vii) clinical screens, etc. Ring resonator-based sensors [17] are of particular interest since they can analyse a wide range of absorption spectra using only a tiny amount of specimens.

Proposed 2DPCRR in the present proposal has a high-quality factor (Q-factor) of 3105.58, and a spectral width of 0.5nm at the resonant wavelength of 1552.79nm. The sensor shows a high figure of merit ($862RIU^{-1}$), a low detection limit ($1.2 * 10^{-4}RIU$), and a maximum sensitivity of 431nm/RIU. The sensor is homogeneous in terms of the positions and radius of the holes and the resonant wavelength shifts almost linearly with the holes' refractive index. The footprint of the proposed 2DPCRR is merely $75\mu m^2$, much smaller compared to the recently published results. The forward dropping efficiency is high which is around 98% at 1552.79nm. The proposed sensor can identify a variety of chemical compounds and therefore can be employed in a range of applications from sensing, switching to filtering. Our structure has been simulated using FDTD and PWE method. FDTD method is used to solve Maxwell's equations in the time domain, whereas the PWE method is used to solve them in the frequency domain [18]. Fabrication processes of PCs structures can be seen elsewhere, e.g. in [19, 20].

Base structure with desirable band diagram

The proposed structure is based on the structure given in the paper [21]. Parameters for the base structure having a desirable band diagram are found in the first step. We start with a PCs slab of the dimension of 29 ∗ 21 with cylindrical air holes arranged in triangular lattices in the X- and Z-directions. The chosen parameters are; lattice constant (a) = 1000nm, a radius of holes (r) = 0.2 ∗ a, the refractive index of the slab (n_1) = 3.4, and the refractive index of holes (n) = 1. With these parameters, a narrow bandgap of $0.012\mu m^{-1}$ is obtained in the range of$0.198 \leq a/\lambda \leq 0.210$. To obtain a wider bandgap, the hole radius is varied and corresponding bandgaps are calculated. The obtained result is as in Fig. 1.

We chose a hole radius equal to 0.295 ∗ a as it results in an adequate PBG in a range useful for realizing the optical sensors (see Fig. 2). Further, the corresponding r/a ensures single-mode light propagation if defect waveguides are created. A larger value of r/a would lead to
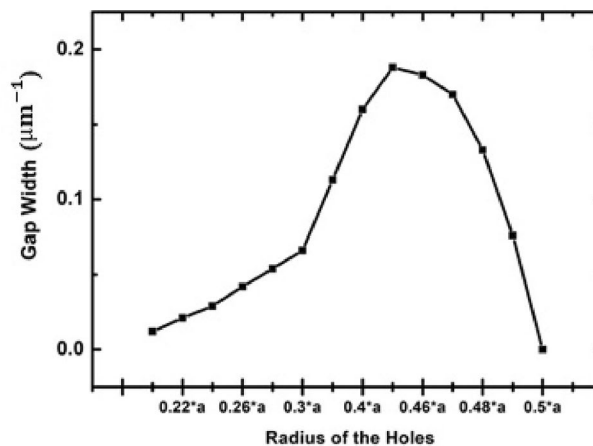

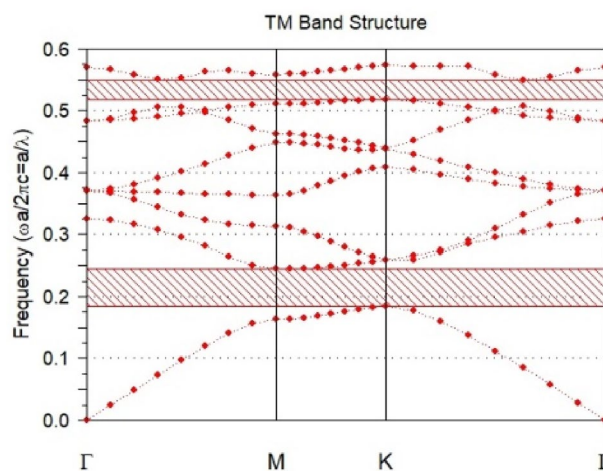**Fig. 1** Variation of bandgap with change in radius of the holes of the considered structure

Fig. 2 The photonic bandgap (for the TM mode) of the structure when the radius of holes is 0.295 ∗ a (other parameters as mentioned in the text) lies in the range $0.183 < a/\lambda < 0.244$ and the second in the range $0.518 < a/\lambda < 0.549$. The first bandgap spans the wavelength range of 1202–1709 nm

undesirable multimode light propagation. The periodic dielectric holes in the slab permit the transverse magnetic (TM) wave, wherein the magnetic field is perpendicular to the plane of the slab. As evident in the figure, the band diagram of the basic structure consists of two PBGs. The first bandgap lies in the range $0.183 \leq a/\lambda \leq 0.244$ and the second in the range $0.518 \leq a/\lambda \leq 0.549$. The first photonic bandgap is of our interest as it spans the wavelength range of 1202–1709 nm.

In what follows, the sensor structure is proposed and analysed. Its parameters are finalized with the following consideration;

1. With the central value of the bandgap equal to $0.213\mu m^{-1}$, the lattice constant should be adjusted to have the operating wavelength of the sensor in the telecommunication range.
2. The ring resonator should have a resonant wavelength in the telecommunication range
3. The refractive index of the slab should be realistic.
4. The sensor should exhibit optimum performance with the chosen parameters.

The sensor

The proposed sensor uses $r = 0.295*a$ same throughout and all holes are spaced with equal periodicity on the slab. There is a hexagonal ring in the middle of the BUS/Input Port and the DROP/Output port, as shown in Fig. 3. The hexagonal ring is created by removing eighteen rods around the centre of the cavity. Fifteen rods are removed to create end linked (with their one end closed) BUS and DROP waveguides. BUS and DROP waveguides are placed on either side of the hexagonal ring forming an optical ring resonator. The resonant wavelength makes multiple round trips, increasing its intensity at the drop port.

Functioning of the sensor is straightforward. The ring allows coupling of the injected light from the input (BUS) waveguide to the output (DROP) waveguide only at a certain wavelength called resonant wavelength (which depends on the geometric and physical parameters of the structure). If light with a wide spectrum is injected into the input port, only resonant wavelength appears at the output. Increase/decrease of the refractive index of the holes results in red/blue shift in the resonant wavelength. If holes are filled with a chemical/biochemical, the chemical/biochemical can be detected by the resultant red or blue shift of a reference resonant wavelength [9].
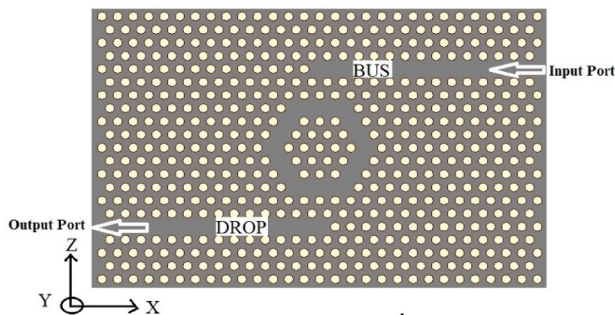

Fig. 3 Schematics design of the chemical/biochemical sensor. A perfectly matched layer of 500nm width has been employed to avoid unwanted back reflections. Grid size of $a/16$ has been considered to perform simulations

Numerical investigations

BandSolve and FullWAVE from RSOFT Design Group, NY-USA, are used for simulations. The dispersion diagram is obtained by solving Maxwell's equation in the frequency domain using PWE method. The proposed structure employs the 2D-FDTD method to study the propagation of the electromagnetic wave in the considered sensor. FDTD solves Maxwell's equation in the time domain (not discussed here for the sake of brevity) [22].

X–Z plane is the plane of propagation. A perfectly matched layer (PML) of 500nm width has been employed to avoid unwanted back reflections [23]. To measure the transmission, a power monitor has been configured at the output port. Gaussian pulse with a broad spectral range is launched at the input (BUS) port, and the transmission spectrum is monitored at the output (DROP) port. The output power is measured using the following equation, where, $T(f)$ denotes the transmission function as a function of wavelength, $p(f)$ denotes the pointing vector, and dS denotes the surface normal [24].

$$T(f) = \frac{1/2 \int \text{real}\left[p(f)^{\text{monitor}}\right]dS}{\text{InputPower}} \quad (1)$$

Choice of proper spatial and temporal grid size is required so that the time step matches the simulation output with a real-time system. A grid size of $a/16 = 22nm$ has been considered to perform simulations and the time step of $\Delta t = 0.01490$ is used in the FDTD simulation, it provides stable output. The time step is calculated by [24]

$$\Delta t \leq \frac{1}{c\sqrt{\frac{1}{(\Delta x)^2} + \frac{1}{(\Delta z)^2}}} \quad (2)$$

where Δt denotes the step time, and c denotes the speed of light in free space, respectively.

The ratio of energy stored to energy lost per cycle is used to calculate the quality factor of a ring resonator. The quality factor (Q) is given by

$$Q = \lambda/\text{FWHM} \quad (3)$$

where λ is the resonance wavelength, and FWHM (Full-width half maximum) is the spectral line width [8].

The sensitivity (S) of the device is the ratio of a shift in resonant wavelength to change in the refractive index of the given sample and is calculated as

$$S = \frac{\Delta\lambda}{\Delta n} \quad (4)$$

where $\Delta\lambda$ is a shift in the resonant wavelength, and Δn is a change in the refractive index of holes [13].

The figure of merit (FOM) [25] defines as the performance/ability of a device to identify any alteration in refractive index.

$$\text{FOM} = \frac{S}{\text{FWHM}} \tag{5}$$

and low detection limit (*DL*) [18] is the minimum refractive index change that can be detected and is given as,

$$\text{DL} = \frac{\lambda}{10 \cdot Q \cdot S} \tag{6}$$

Structure parameters are optimized to obtain (i) resonant wavelength in the telecommunication wavelength range, (ii) a small value of FWHM with high transmission (high Q-factor) for high sensitivity, (iii) a high figure of merit, and (iv) a low detection limit.

To understand the behaviour of the considered structure and/or to know the most suited parameters, the effect of variation of (i) lattice constant and (ii) radius of the holes on normalized transmission is investigated. Having all other parameters finalized, the effect of variation of the refractive index of holes (*n*) using various chemicals at 1550nm on the normalized transmission is investigated to see the sensitivity/performance of the device.

Effect of variation of lattice constant

In this section, effect of variation of lattice constant (*a*) on the normalized transmission is investigated. The chosen set of parameters is $r = 2.95 * a$, $n = 1$. The slab refractive index is chosen to be 3.46 as it is the refractive index of silicon and we found it results in high coupling. The lattice constant is altered in the steps of 1nm. As can be seen in Fig. 4, the lattice constants of 351nm, 352nm, and 353nm yield resonant peaks at 1547.99nm, 1552.79nm, and 1556.82nm, respectively, indicating a red shift in the resonant peak with an increase in the lattice constant. Table 1 demonstrates the sensor's performance as the lattice constant is varied.

It can be seen that on increasing the lattice constant, the quality factor increases, while the spectral line width remains constant. The lattice constant of 352nm is of our interest as it corresponds to the wavelength of 1552.79nm (telecommunication range). It is found that 1nm of change in the lattice constant results in a wavelength shift of 4.8nm.

Effect of variation of holes' radius

Though the radius of the holes is already fixed at $0.295 * a$ in the previous sections, for the sake of understanding performance behaviour, the effect of variation of holes' radius on the normalized transmission is investigated in this section. The set of parameters for this section is $a = 352\text{nm}$,
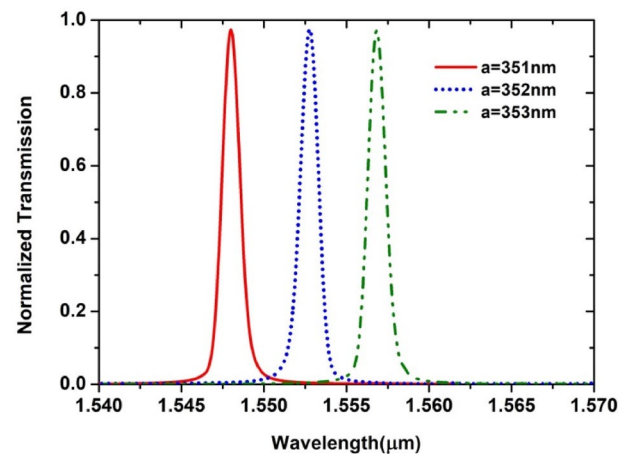

Fig. 4 Normalized transmission spectra when the lattice constant is chosen to be 351nm, 352nm, and 353nm and the corresponding resonant wavelengths are 1547.99nm, 1552.79nm, and 1556.82nm, respectively

Table 1 Performance of the sensor on varying the lattice constant

Sl. no	Lattice constant (a)(nm)	Resonant wavelength (nm)	Transmission (%)	Spectral linewidth (nm)	Quality factor
1	351	1547.99	98	0.5	3095.98
2	352	1552.79	98	0.5	3105.58
3	352	1556.82	98	0.5	3113.64

$n_1 = 3.46$, and $n = 1$. The holes' radius is varied with an increment of $0.05 * a$. For holes' radius equal to $0.29 * a$, $0.295 * a$, and $0.3 * a$, resonant peaks are obtained at 1560.06nm, 1552.79nm, and 1545.59nm, respectively, as shown in Fig. 5. Table 2 depicts the sensor's performance as the radius of the holes is varied.

On increasing the radius of the holes, a blue shift in resonance wavelength is observed. As can be seen in Fig. 5, a resonant wavelength of 1552.79nm with a spectral linewidth of 0.5nm is obtained at the holes' radius of $0.295 * a$. Further, a high transmission of 98% and quality factor of 3105.58 are also observed. Our investigation revealed that the change of $0.05 * a$ in hole radius results in 7.27nm of wavelength shift.

Sensor performance

Having structural parameters finalized in the previous sections, this section is devoted to investigating the overall performance of the proposed sensor by varying the refractive index of holes and observing the effect on the normalized transmission. The finalized set of parameters is $a = 352\text{nm}$, $r = 0.295 * a$, $n_1 = 3.46$.
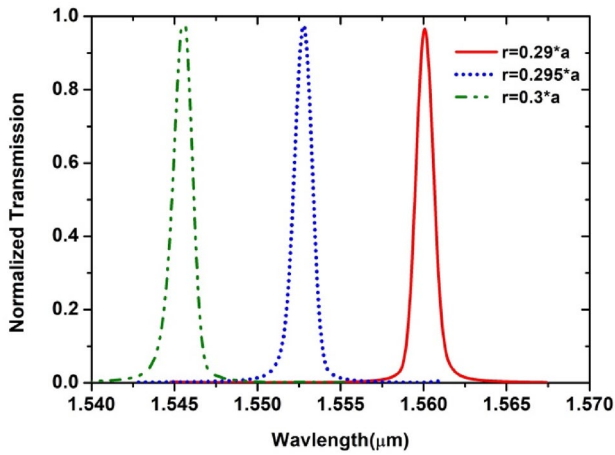
Fig. 5 Normalized transmission spectra when the radius of the holes is chosen to be $0.29 * a, 0.295 * a$, and $0.3 * a$ and the corresponding resonant wavelengths are 1560.06nm, 1552.79nm, and 1545.59nm, respectively

Table 2 Performance of the sensor on varying the radius of the holes

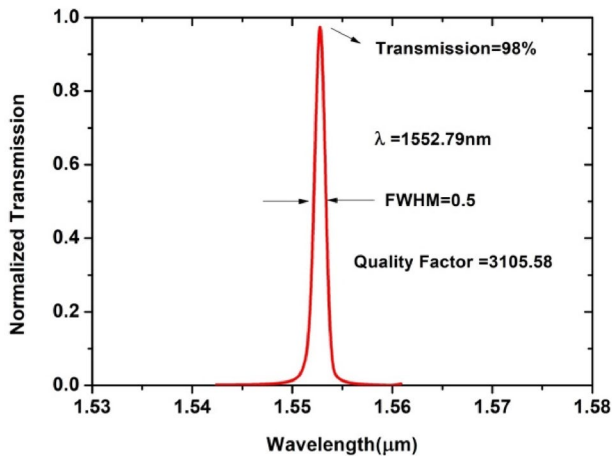| Sl. no	Radius of holes (r)(nm)	Resonant wavelength(nm)	Transmission(%)	Spectral linewidth (nm)	Quality factor
1	0.29*a	1560.06	98	0.5	3120.12
2	0.295*a	1552.79	98	0.5	3105.58
3	0.3*a	1545.59	98	0.5	3091.18

Fig. 6 Normalized transmission at a resonant wavelength of $1552.79nm$ when the background is air ($n = 1$). The optimum values, for instance, $a = 352nm, r = 0.295 * a, n_1 = 3.46$, and slab thickness of 219nm are chosen for simulations. High transmission of 98 %, a high-quality factor of 3105.58, and small spectral width (FWHM) of 0.5nm have been obtained

As shown in Fig. 6, the dropping efficiency (normalized transmission at the output port) at the resonant wavelength is 98%. The computed quality factor and spectral line width of the proposed ring resonator are 3105.58 and 0.5nm, respectively, which are desirable values for sensing any chemical and biological analytes. The proposed sensor shows high sensitivity (431nm/RIU), low DL ($1.2 * 10^{-4}$RIU), and high FOM(862RIU^{-1}). It is easily anticipated from the Fig. 6 that if an optical input is injected in to the input port of the sensor structure at the resonant wavelength (1552.79 nm), it would show appreciable transmission, while, an optical input of wavelengths sufficiently away from the resonant wavelength (off-resonant wavelengths) would show zero or negligible transmission. The same is confirmed in Fig. 7a and 7b, wherein optical propagation in the sensor structure is shown through magnetic field profiles. Figure 7a shows the optical propagation for injection of optical wavelength of 1552.79 nm, while Fig. 7b shows the same for the optical wavelength of 1550 nm.

We also investigated the chemical sensitivity and performance of the device. Numerous organic/ chemical compounds can be detected by the proposed chemical/biochemical sensor. Table 3 presents some of the findings. The considered values of the refractive indices (at 1550nm) of deionized water and a range of chemicals (Anhydrous Ethanol, Isopropanol, Ethylene Glycol, Chloroform, Glycerol) are taken from [26].

The normalized transmission spectrum of the proposed sensor for holes' refractive indices corresponding to water and a variety of chemical compounds is shown in Fig. 8 in the wavelength range of 1.68μm to 1.76μm. The proposed sensor shows maximum sensitivity of 431nm/RIU.

It is also revealed, as shown in Fig. 9, that the resonance wavelength shifts linearly as the holes' refractive index changes which are highly desirable. The sensor's performance is evaluated in the presence of water and a few of the chemical compounds listed in Table 3. A comparison of the proposed sensor with various PCs designs is shown in Table 4.

Conclusion

A label-free chemical/biochemical sensor based on 2DPCRR created by periodic holes in the slab is designed in this paper. The design consists of a hexagonal ring resonator. The geometrical/physical parameters of the proposed sensor are optimized, and the optimization procedure is discussed in brief. The ring resonator of the sensor resonates at the wavelength of 1552.79nm exhibits high transmission of 98%, high-quality factor (3105.58) and narrow spectral width (0.5nm). The proposed sensor shows a high figure of merit (862RIU^{-1}) and a low detection limit

Fig. 7 Magnetic field profile for **a** on-resonance wavelength of 1552.79nm and **b** off-resonance wavelength of 1555nm. The red and blue colour represents the positive and negative magnetic field, while the green colour represents the silicon slab. The black outline shows the air holes
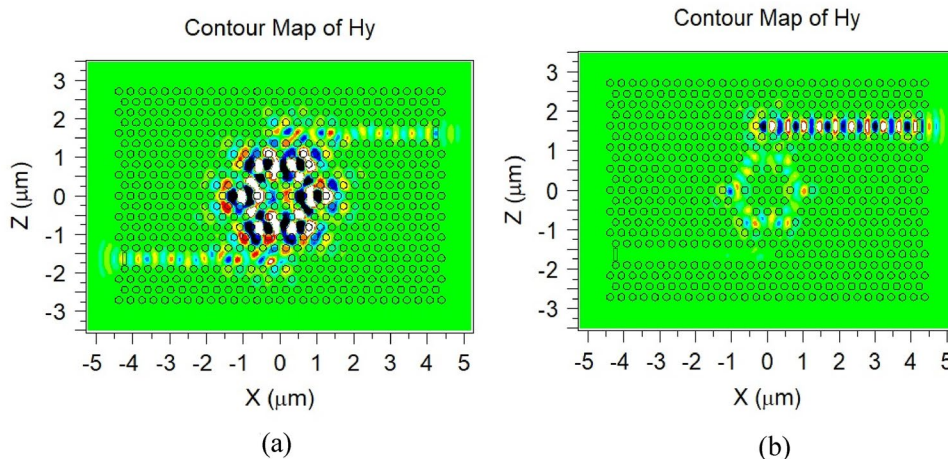

(a)

(b)

Table 3 Performance of chemical/biochemical sensor

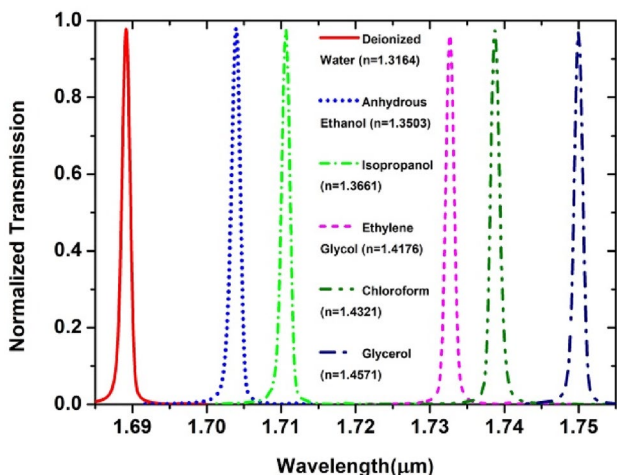| Hole-filling substance	Refractive index (n) (1550 nm) at 298 K[26]	Change in refractive index (Δn)	Resonant wavelength (λ)(nm)	The shift in resonant wavelength ($\Delta \lambda$) (nm)	Sensitivity($S = \frac{\Delta \lambda}{\Delta n}$)
Deionized water	1.3164	–	1689.19	–	–
Anhydrous ethanol	1.3503	0.0339	1703.99	14.8	436.57
Isopropanol	1.3661	0.0158	1710.66	6.67	422.15
Ethylene glycol	1.4176	0.0515	1732.67	22.01	427.37
Chloroform	1.4321	0.0145	1738.70	6.03	415.86
Glycerol	1.4571	0.0250	1750.00	11.3	452.00

Fig. 8 Depicts the normalized transmission spectrum of the proposed sensor for holes' refractive indices corresponding to water, and a variety of chemical compounds in the wavelength range of 1.68μm to 1.76μm. The proposed sensor shows maximum sensitivity of 431nm/RIU
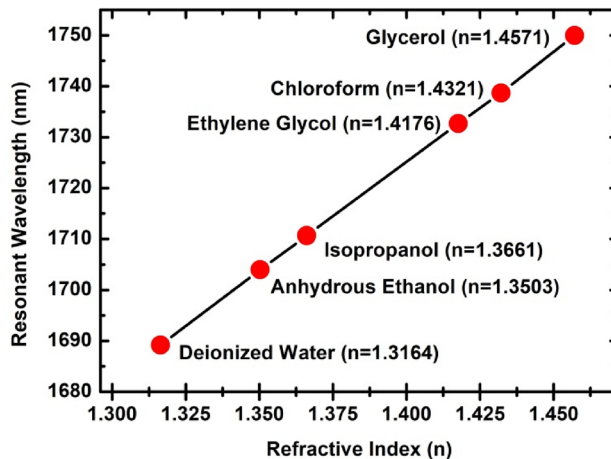

Fig. 9 Shifts in the resonant wavelength as a result of variations in the refractive indices of a variety of chemical substances

($1.2 * 10^{-4}$RIU). The sensor exhibits a maximum sensitivity of 431nm/RIU. The structure in the present proposal is

homogeneous in terms of the holes' positions and radius; moreover, the resonant wavelength shifts linearly as the holes' refractive index changes which are highly desirable features. The footprint of the proposed 2DPCRR is merely 75μm², much smaller compared to the recently published results. The proposed sensor can identify a variety of

Table 4 Comparison of the proposed sensor with various PCs designs

Reference	Year	Sensitivity (nm/RIU)	Detection limit (RIU)	Figure of merit (RIU^{-1})	Quality factor	Footprint (μm^2)
[27]	2019	501.88	–	–	749.58	250.24
[28]	2019	–	–	–	2210.00	383.89
[29]	2019	–	–	–	2583.50	174.24
[30]	2021	–	–	0.97	3288.00	104.35
[24]	2021	–	–	–	2337.00	412.76
[31]	2023	166	$1.4 * 10^{-4}$	392.5	3702.00	515.29
This work		431	$1.2 * 10^{-4}$	862	3105.58	75

chemical compounds and therefore can be employed in a range of applications from sensing and switching to filtering.

References

1. M. Notomi, Manipulating light with strongly modulated photonic crystals. Rep. Prog. Phys. (2010). https://doi.org/10.1088/0034-4885/73/9/096501
2. S.G. Johnson, A. Mekis, S. Fan, J.D. Joannopoulos, Molding the flow of light. Comput. Sci. Eng. **3**(6), 38–47 (2001). https://doi.org/10.1109/5992.963426
3. U.K. Khankhoje et al., Modelling and fabrication of GaAs photonic-crystal cavities for cavity quantum electrodynamics. Nanotechnology (2010). https://doi.org/10.1088/0957-4484/21/6/065202
4. J.E. Baker, R. Sriram, B.L. Miller, Two-dimensional photonic crystals for sensitive microscale chemical and biochemical sensing. Lab Chip **15**(4), 971–990 (2015). https://doi.org/10.1039/c4lc01208a
5. D. Threm, Y. Nazirizadeh, M. Gerken, Photonic crystal biosensors towards on-chip integration. J. Biophotonics **5**(8–9), 601–616 (2012). https://doi.org/10.1002/jbio.201200039
6. Y. Zhang, Y. Zhao, R. Lv, A review for optical sensors based on photonic crystal cavities. Sens. Actuators A Phys. (2015). https://doi.org/10.1016/j.sna.2015.07.025
7. M.A. Lifson, B.L. Miller, Photonic crystals as robust label-free biosensors. Springer Ser. Mater. Sci. **229**, 189–207 (2015). https://doi.org/10.1007/978-3-319-24990-2_7
8. P. Sharma, M. Mohan, N. Ghosh, S. Medhekar, Materials today: proceedings 2D photonic crystal based all-optical add-drop filter consisting of square ring resonator. Mater. Today Proc. (2022). https://doi.org/10.1016/j.matpr.2022.07.062
9. Y. Liu, H.W.M. Salemink, Photonic crystal-based all-optical on-chip sensor. Opt. Express **20**(18), 27930–27937 (2012)
10. S. Norouzi, K. Fasihi, Realization of pressure sensor based on a GaAs-based two dimensional photonic crystal slab on SiO2 substrate. J. Comput. Electron. (2022). https://doi.org/10.1007/s10825-022-01861-5
11. M.R. Lee, P.M. Fauchet, Two-dimensional silicon photonic crystal based biosensing platform for protein detection. Opt. Express **15**(8), 4530 (2007). https://doi.org/10.1364/oe.15.004530
12. Y. Wu, Y. Zhou, J. Pan, T. Huang, S. Jin, Jou rna lP. Opt. Commun. (2023). https://doi.org/10.1016/j.optcom.2023.129288
13. P. Sharma, S. Medhekar, Ultra-compact photonic crystal nano-cavity-based sensor for simultaneous detection of refractive index and temperature. J. Opt. (2022). https://doi.org/10.1007/s12596-022-01037-1
14. N. Ghosh, P. Sharma, S. Medhekar, and M. M. Gupta, Design and analysis of the pressure sensor based on 2D photonic crystal consisting of micro-cavity. in 2021 IEEE international conference on technology, research, and innovation for betterment of society (TRIBES). **978**, 6654–3342 (2021). 10.1109/ TRIBE S52498. 2021. 97516 78
15. J. Wang, S.X. Chew, S. Song, L. Li, L. Nguyen, X. Yi, On-chip simultaneous measurement of humidity and temperature using cascaded photonic crystal microring resonators with error correction. Opt. Express **30**(20), 35608 (2022). https://doi.org/10.1364/oe.466362
16. F. Fathi, M.R. Rashidi, P.S. Pakchin, S. Ahmadi-Kandjani, A. Nikniazi, Photonic crystal based biosensors: emerging inverse opals for biomarker detection. Talanta **221**, 121615 (2021). https://doi.org/10.1016/j.talanta.2020.121615
17. P. Sharma, M. M. Gupta, N. Ghosh, and S. Medhekar, Optical add-drop filter based on square ring resonator consisting of octagon shape core. in: 2021 IEEE international conference on technology, research, and innovation for betterment of society (TRIBES). **978**, 6654–3342 (2021). 10. 1109/ TRIBE S52498. 2021. 97516 37
18. A. Benmerkhi, A. Bounouioua, M. Bouchemat, T. Bouchemat, Analysis of a photonic crystal temperature sensor based on Z-shaped ring resonator. Opt. Quantum Electron. **53**(1), 1–14 (2021). https://doi.org/10.1007/s11082-020-02730-w
19. S. Kedia, R. Vijaya, Photonic crystal waveguides by direct writing of e-beam on self-assembled photonic crystals. Bull. Mater. Sci. **34**(2), 383–388 (2011). https://doi.org/10.1007/s12034-011-0063-y
20. H. Schift et al., Fabrication of polymer photonic crystals using nanoimprint lithography. Nanotechnology (2005). https://doi.org/10.1088/0957-4484/16/5/023
21. F.L. Hsiao, C. Lee, Computational study of photonic crystals nano-ring resonator for biochemical sensing. IEEE Sens. J. **10**(7), 1185–1191 (2010). https://doi.org/10.1109/JSEN.2010.2040172
22. J. B. Schneider, Understanding the finite-difference time-domain method, (2022)
23. J.P. Berenger, A perfectly matched layer for the absorption of electromagnetic waves. J. Comput. Phys. **114**(2), 185–200 (1994). https://doi.org/10.1006/jcph.1994.1159
24. M. Radhouene, V.R.B. Monia, S.R.V. Janyani, Rounded square ring resonator based add drop filter for WDM

applications using two dimensional photonic crystals. Opt. Quantum Electron. **53**(5), 1–24 (2021). https://doi.org/10.1007/s11082-021-02924-w

25. C. Malek et al., High performance biosensor composed of 1D defective photonic crystal for sensing and detection of distinguished blood components. Opt. Quantum Electron. (2023). https://doi.org/10.1007/s11082-022-04460-7

26. J.E. Saunders, C. Sanders, H. Chen, H.-P. Loock, Refractive indices of common solvents and solutions at 1550 nm. Appl. Opt. **55**(4), 947 (2016). https://doi.org/10.1364/ao.55.000947

27. R. Rajasekar, S. Robinson, Nano-pressure and temperature sensor based on hexagonal photonic crystal ring resonator. Plasmonics **14**(1), 3–15 (2019). https://doi.org/10.1007/s11468-018-0771-x

28. R. Massoudi, M. Najjar, F. Mehdizadeh, V. Janyani, Investigation of resonant mode sensitivity in PhC based ring resonators. Opt. Quantum Electron. (2019). https://doi.org/10.1007/s11082-019-1793-0

29. R. Rajasekar, J.K. Jayabarathan, S. Robinson, Nano-optical filter based on multicavity coupled photonic crystal ring resonator. Phys. E Low-Dimens. Syst. Nanostruct. **114**, 113591 (2019). https://doi.org/10.1016/j.physe.2019.113591

30. M. Hosseinzadeh Sani, H. Saghaei, M.A. Mehranpour, A. AsgariyanTabrizi, A novel all-optical sensor design based on a tunable resonant nanocavity in photonic crystal microstructure applicable in mems accelerometers. Photonic Sens. **11**(4), 457–471 (2021). https://doi.org/10.1007/s13320-020-0607-0

31. B. Krishnamoorthi, B. Elizabeth Caroline, M. Michael, S. Thirumaran, A novel rhombic shaped photonic crystal bio-sensor for identifying disorders in the blood samples. Opt. Quantum Electron. (2023). https://doi.org/10.1007/s11082-023-04584-4